Flexible construction of heteroatom-free g-C$_3$N$_4$/g-C$_3$N$_4$ homojunction with switching charge dynamics toward efficient photo-piezocatalytic performance

Huanhuan Zhai [a], Hongqin Liu [a], Yi Zhang [a], Jiaxin Tong [a], Xinfeng Liu [b,c], Wenna Du [b,c,*], Hanxiao Liao [d,**], Pengfei Tan [a], Jun Pan [a,**]

[a] State Key Laboratory of Powder Metallurgy, Central South University, Changsha 410083, PR China
[b] CAS Key Laboratory of Standardization and Measurement for Nanotechnology, National Center for Nanoscience and Technology, Beijing 100190, PR China
[c] University of Chinese Academy of Sciences, Beijing 100190, PR China
[d] School of Metallurgy and Environment, Central South University, Changsha 410083, PR China

ARTICLE INFO

ABSTRACT

Photo-piezocatalysis based on homojunction emerges as an auspicious approach for the environmental crisis, while it is still in early stage with limited strategies and ambiguous reaction mechanisms. Herein, a heteroatom-free homojunction of ultrathin g-C$_3$N$_4$ with N vacancies/pristine g-C$_3$N$_4$ has been innovatively constructed through surface coupling effect. It achieves higher performance on both photo-piezocatalytic RhB degradation and H$_2$O$_2$ production than solely piezocatalysis or photocatalysis. The underlying causes lie in the synergistic effects of the internal electric field constructed in the type II homojunction and the polarized electric field stimulated by the non-centrosymmetric structure, which cooperatively facilitate the driving force of the charge carriers. Notably, due to the unfixed polarization direction, the charge transfer pathways undergo transitions between type-II and Z-scheme mechanisms, which both promote the spatial separation and migration dynamics of electrons and holes. This work provides new insights into structural design and mechanism exploration for highly efficient photo-piezocatalytic applications.

1. Introduction

The field of photocatalysis has emerged as a critical area of research due to its potential to revolutionize various industries, including environmental remediation, energy conversion, and chemical synthesis [1, 2]. Nevertheless, the conversion efficiency has been limited by insufficient light absorption efficiency, high recombination rates of charge carriers, and the inherent instability of catalysts [3]. Even though various strategies have been explored, such as encompass the fine-tuning of the composition and morphology, the incorporation of metal or non-metal dopants, as well as the construction of composite structures [4,5], the exploitation of highly efficient photocatalysts still holds significant potential for further exploration. Additionally, the piezoelectric effect is a physical phenomenon where mechanically deformed piezoelectric materials convert mechanical energy into electrical energy [6,7]. In the process of piezocatalysis, the generated electric field drives the delivery of free electrons and holes to the material surface under mechanical stress. However, compared with photocatalysis, the piezocatalytic activity has yet reached a satisfactory level, which restricts its widespread practical application [8]. In recent years, there has been a widespread focus on harnessing photo-piezocatalysis for developing a high-performing catalytic approach, which opens new avenues for promoting the process of sustainable and energy-efficient technologies [9,10].

Polarization often occurs in non-centrosymmetric materials, forming a spontaneous electric dipole moment within the material [11]. So far, some non-centrosymmetric semiconductors including CdS, BaTiO$_3$, BiVO$_4$, ZnO et al. have been investigated for photo-piezocatalysis [12–15]. Nevertheless, their wide-bandgap properties limit the responsiveness solely to ultraviolet light, which is merely 4% of the available

---

* Corresponding author at: CAS Key Laboratory of Standardization and Measurement for Nanotechnology, National Center for Nanoscience and Technology, Beijing 100190, PR China.
** Corresponding authors.
E-mail addresses: duwn@nanoctr.cn (W. Du), hxliao@csu.edu.cn (H. Liao), jun.pan@csu.edu.cn (J. Pan).

solar energy spectrum [16]. To effectively address these issues, the metal-free graphitic carbon nitride (g-C$_3$N$_4$) has gathered wide interest because of its appropriate band-gap energy (~2.7 eV), superior physicochemical stability and environment-friendly [17,18]. Even though its centrosymmetrical structure impedes the generation of sufficient piezoelectric charges for promoting piezocatalytic reactions, a few methods have been explored to especially increase the polarity of g-C$_3$N$_4$ in recent. Wherein modifying the layer structure of g-C$_3$N$_4$ is a vital tactic to enhance its piezoelectric response. Cheng et al. constructed atomically thin sheet-like structure of g-C$_3$N$_4$, whose piezoelectricity was stemmed from the superimposed polar tri-s-triazine units and flexoelectric effect originated from the structured triangular cavities [19]. Liu and Ma et al. introduced N vacancies into g-C$_3$N$_4$ nanosheets, and Vuong et al. established the alkaline-earth metals and chlorides co-doped porous g-C$_3$N$_4$ nanosheets, which all aimed to increase the polarity of g-C$_3$N$_4$ layers [20,21]. Moreover, the fabrication of homojunction is a worthwhile tactic to stimulate the piezoelectricity for simultaneous photo-piezocatalysis. The matched electronic and chemical structures of homojunction effectively facilitate the interface separation and transfer of charge carriers, leading to consecutive band bending and the avoidance of lattice distortion drawbacks [22,23]. Tang et al. reported that the homojunction of g-C$_3$N$_4$/PDI-g-C$_3$N$_4$ facilitates the photoelectron transfer at the interfaces, which exhibits superior photo-piezocatalytic atrazine degradation and H$_2$O$_2$ production performance [24]. Xu et al. proposed the crystalline g-C$_3$N$_4$/g-C$_3$N$_{4-x}$S$_x$ isotype heterostructure, and introduced extra cyano groups with removing partial -NH$_x$ species in its tri-s-triazine layer structure, which could significantly intensify the asymmetric structure of g-C$_3$N$_4$ [25]. Although preliminary explorations have been made on photo-piezocatalysis of g-C$_3$N$_4$, the development of heteroatom-free g-C$_3$N$_4$ homojunction with flexible fabrication method has yet to be initiated. Moreover, the current ambiguous photo-piezocatalytic mechanism is extremely imperative to be refined in the pursuit of scientific progress.

By exploiting the morphological variability and bandgap adjustability of g-C$_3$N$_4$, a novel homojunction involving ultrathin g-C$_3$N$_4$ with N vacancies and pristine g-C$_3$N$_4$, combined through surface coupling effect, was fabricated by facile mixing and calcining. Femtosecond time resolved spectroscopy (fs-TAS) confirms the separation and delivery directions of photo-excited charge carriers under the internal electric field (IEF). Piezo-response force microscopy (PFM) proves the generated polarized electric field (PEF) arising from the asymmetric structure. Quenching experiments reveal the reactive species and propose the reaction process of RhB degradation and H$_2$O$_2$ production. Under the dual-field coupling effect, the photo-piezocatalytic RhB degradation and H$_2$O$_2$ production achieves higher performance than that of individual piezocatalysis or photocatalysis. The switching charge transfer pathway between type II and Z-scheme mechanisms is proposed as the inner reason for the efficient charge separation and migration. This work holds significant implications for the development of photo-piezocatalysts with facile fabrication processes and high-efficiency.

2. Experimental

2.1. Preparation of pristine g-C$_3$N$_4$ and ultrathin g-C$_3$N$_4$

Pristine g-C$_3$N$_4$ (PCN) was prepared by a simple polymer condensation method. In detail, 3 g melamine (AR, 99%) was added into a covered crucible and heated at 550 ℃ for 4 h at 2.3 ℃ min^{-1}. After grinding, washing and drying, the bright yellow PCN was obtained. Thereafter, 1.5 g PCN was transferred into the alumina ark (9 cm×6 cm×2 cm), spread it evenly, and then calcined at 520 ℃ for 2 h at 3 ℃ min^{-1}. After cooling down, the ultrathin g-C$_3$N$_4$ (UCN) was obtained, which presented milk white color and loose morphology.

2.2. Preparation of UCN/PCN homojunction

Different ratios of UCN and PCN with the total amount of 200 mg were dispersed separately into 30 mL methanol solutions (AR, 99.5%). Then they were subjected to ultrasound for 4 h. Afterward the suspensions of PCN were transferred to the UCN solution and stirred at room temperature until the methanol completely evaporated. After drying at 60 ℃ for 12 h, the powder was transferred to muffle and calcined at 300 ℃ for 2 h. Finally, the homojunctions were obtained and labeled as HCN-x (x=1, 2, 3), where the ratios of UCN and PCN were 4:1, 2:1 and 1:1, respectively. Otherwise, 200 mg UCN or PCN was treated in the same procedure with HCN-x, which was abbreviated as UCN-T or PCN-T. For comparison with the homogeneous, pure UCN, pure PCN and the mixture of UCN/PCN (MCN-1, MCN-2 and MCN-3) were synthesized by ultrasonic treating and stirring the mixture for only 1 h. After centrifuging and drying, the targeted powder was achieved.

2.3. Catalyst characterization

The morphology and structure characterization of the prepared samples were performed by TEM, AFM, XRD, BET, XPS, FT-IR, ESR, PL, UV-Vis absorption spectra and photoelectrochemical experiments. The details are described in Text S1 of the Supplementary Materials.

2.4. Transient absorption measurements

fs-TAS were conducted to analysis the transport dynamics of charge carriers. The details of the instrument parameter are provided in Text S2 of the Supplementary Materials.

2.5. Piezo-photocatalytic performance

Piezo-photocatalytic RhB degradation and H2O2 production were carried out to evaluate the catalyst performance. The details are listed in Text S3 of the Supplementary Materials.

3. Results and discussion

3.1. Catalysts characterization

The synthesis procedure of HCN-x, (x=1, 2, 3) is exhibited in Fig. 1a. Wherein, PCN and UCN were fabricated by polymer condensation and thermal exfoliation methods in succession. As evidenced by transmission electron microscopy (TEM) images (Fig. S1), PCN exhibits tightly stacked and curly structure. Whereas UCN displays few-layers and smooth surface, which is attributed to the weakened interlayer binding force of van der Waals and strong covalent C-N bonds remain in each layer during the second calculation process [26]. Subsequently, HCN-x was prepared by stirring the mixture of UCN and PCN and then calcining at 300 ℃ for 2 h. Under the action of centrifugal force during the stirring process, PCN and UCN could be uniformly dispersed and closely contacted. The following calcination facilitates the formation of robust junction at the interface. For comparison, solely UCN or PCN were treated likewise, which is abbreviated as UCN-T or PCN-T. TEM images reveal that UCN-T exhibits a huge surface area layer without obvious winkle, while PCN-T still remains a piled structure like PCN (Fig. 1b and c). For HCN-1, the highly tiled UCN serves as the support for the randomly distributed PCN, indicating successful construction of UCN/PCN homojunction with close contact (Fig. 1d). The thickness of UCN-T and PCN-T is 1.450 nm and 5.144 nm, as confirmed by atomic force microscopy (AFM), which comprise 4–5 at. layers for UCN-T and 15–16 at. layers for PCN-T (Fig. S2). The specific surface areas of UCN-T, HCN-1, HCN-2, HCN-3 and PCN-T are 95.48, 93.17, 82.24, 84.87 and 24.27 m^2 g^{-1}, individually (Fig. S3a). Meanwhile, the pore diameter of the fabricated catalysts is mainly distributed at 3.5–3.8 nm (Fig. S3b). The X-ray diffraction (XRD) patterns and the enlarged peaks of (002)
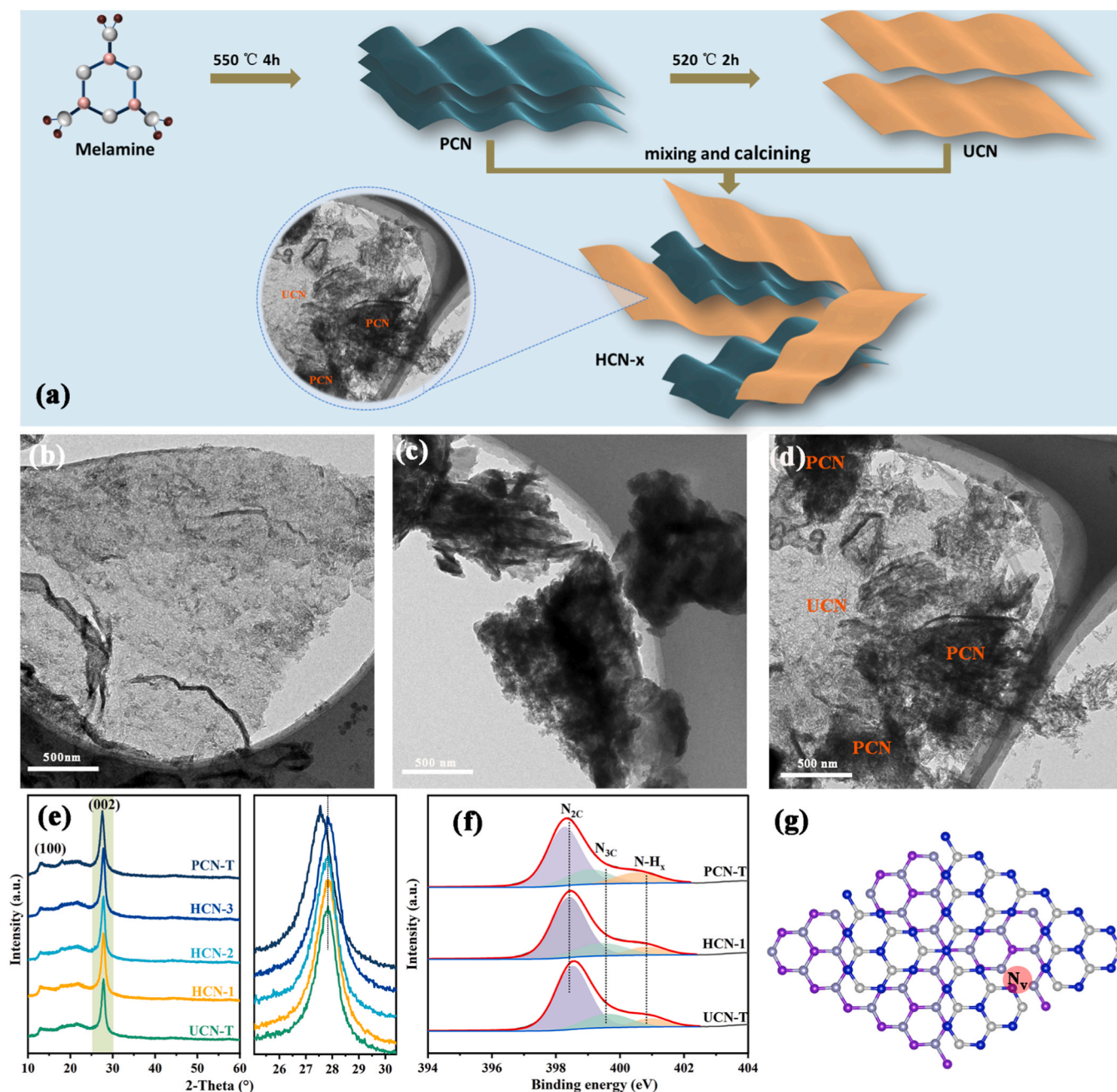
Fig. 1. (a) Schematic preparation process of HCN-x. TEM images of (b) UCN-T, (c) PCN-T and (d) HCN-1. (e) XRD patterns of UCN-T, HCN-x and PCN-T. (f) XPS spectra of N 1 s for PCN-T, HCN-1 and UCN-T. (g) The structure schematic of HCN-1. (The light grey and blue balls represent C and N atoms for PCN. The dark grey and purple balls represent C and N atoms for UCN).

are shown in Fig. 1e. Typical characteristic peaks of g-C$_3$N$_4$ are located at around 13° and 27°, which are affiliated with the in-plane structural packing motif of the tri-s-triazine unit and interlayer stacking, respectively [27]. Obviously, the (002) peaks of UCN-T and HCN-x are positioned at 27.8° without any shift, which are evidently higher than that of PCN-T. The angle of (002) peaks for UCN-T and HCN-x reflect an interlayer distance of 0.320 nm on the basis of d = λ/2sinθ. However, this peak of PCN-T at 27.5° gives an interlayer distance of 0.323 nm. The lower d-spacing of UCN-T is ascribed to the flat surface with decreased layer spacing. Particularly, the introduction of PCN into the homojunction has no influence on the interlayer distance, demonstrating a tight contact between PCN and UCN in HCN-x is constructed through the surface coupling effect. For comparison, the XRD patterns for the mixture of UCN and PCN (MCN-x, x=1, 2, 3) were prepared (Fig. S4). As

the amount of PCN gradually increases, the (002) peaks of MCN-x progressively shift closer to that of pure PCN. It suggests that UCN and PCN are not tightly coupled in the mixture. Fourier transform infrared (FT-IR) spectra in Fig. S5 exhibit typical peaks of g-C$_3$N$_4$, indicating the graphitized structure framework is well-preserved within the homojunctions [28]. Especially, compared with UCN-T and PCN-T, the stretching vibrations of aromatic C-N rings between 1200 and 1700 cm^{-1} are distinctly higher and become increasingly pronounced for HCN-x with the gradual introduction of PCN. This occurrence can be attributed to the surface coupling effect between PCN and UCN, resulting in a larger net change in molecular dipole moment and an augment of the asymmetry [29].

X-ray photoelectron spectroscopy (XPS) was proceeded to confirm the chemical information on the catalysts surface (Fig. 1f). Three main

peaks at 398.4 eV, 399.5 eV, and 400.8 eV are partitioned on N 1 s spectrum of HCN-1, affiliating to sp^2-hybridized nitrogen $N_{2\,C}$, $N_{3\,C}$, and amino groups $N-H_x$, respectively. The C 1 s spectra exhibit three fitted peaks with the binding energy of 284.8, 286.3 eV and 288.0 eV for HCN-1, which are affiliated to C-C, N=C-N and N=C-N (Fig. S6). Interestingly, the fitted peaks of N 1 s and N=C-N peak of C 1 s for HCN-1 are located between UCN-T and PCN-T, which implies the establishment of a charge transfer channel within the homojunction of UCN and PCN through surface coupling effects [30,31].What's more, the area percentages of all fitted peaks for N 1 s are listed in Table S1. The medium ratio of HCN-1 further proves the successful construction of UCN/PCN homojunction. In pursuit of elucidating the internal structural information of the homojunction, XPS analysis was carried out on UCN and PCN (Fig. S7a). The area ratio of $N_{2\,C}$ to $N_{3\,C}$ in the N 1 s fitting peak is determined to be 3.397 for PCN, whereas a drastic reduction to 1.286 is observed for UCN. Owing to the relative stability of $N_{3\,C}$ in the tri-s-triazine structure of g-C_3N_4, this significant decrease can be attributed to the loss of N atoms at $N_{2\,C}$ for UCN during the secondary annealing process. Furthermore, electron spin resonance spectra (ESR) were conducted to explore the spin state of the lone pair electrons. Remarkably, the peak intensity of UCN surpass that of PCN, further corroborating the existence of vacancies (Fig. S7b). Based on these findings, the proposed structure of HCN-1 homojunction is depicted as shown in Fig. 1g.

3.2. Photoelectrical and piezoelectric analysis

The Photoluminescence (PL) spectra reveal the validity quenched peak intensity of HCN-1 in comparison with UCN-T and PCN-T, demonstrating the effectively impaired recombination efficiency of charge carriers in the homojunction [32] (Fig. 2a). Transient fluorescence spectra in Fig. 2b reveal that the average lifetimes of UCN-T, HCN-1 and PCN-T are 4.1989, 4.5221, 2.8028 ns, separately. The longer lifetime of HCN-1 indicates that the combination of UCN and PCN effectively increases the lifetime of the charge carriers. The photocurrent (IT) responses evident that the current density of HCN-1 is relatively higher than the other four samples, indicating an enhanced separation rate of photo-induced carriers for HCN-1 (Fig. S8). Optical properties of UCN-T, HCN-1 and PCN-T were examined by UV-Vis absorption spectra (Fig. 2c). It is clear to find that the absorption band edges of UCN-T, HCN-1 and PCN-T are 460, 462 and 467 nm, respectively. The absorption edge of HCN-1 still remains at the middle position between UCN-T and PCN-T, representing the middle level of the minimum energy required for light absorption [30,33]. It is attributed to the electronic
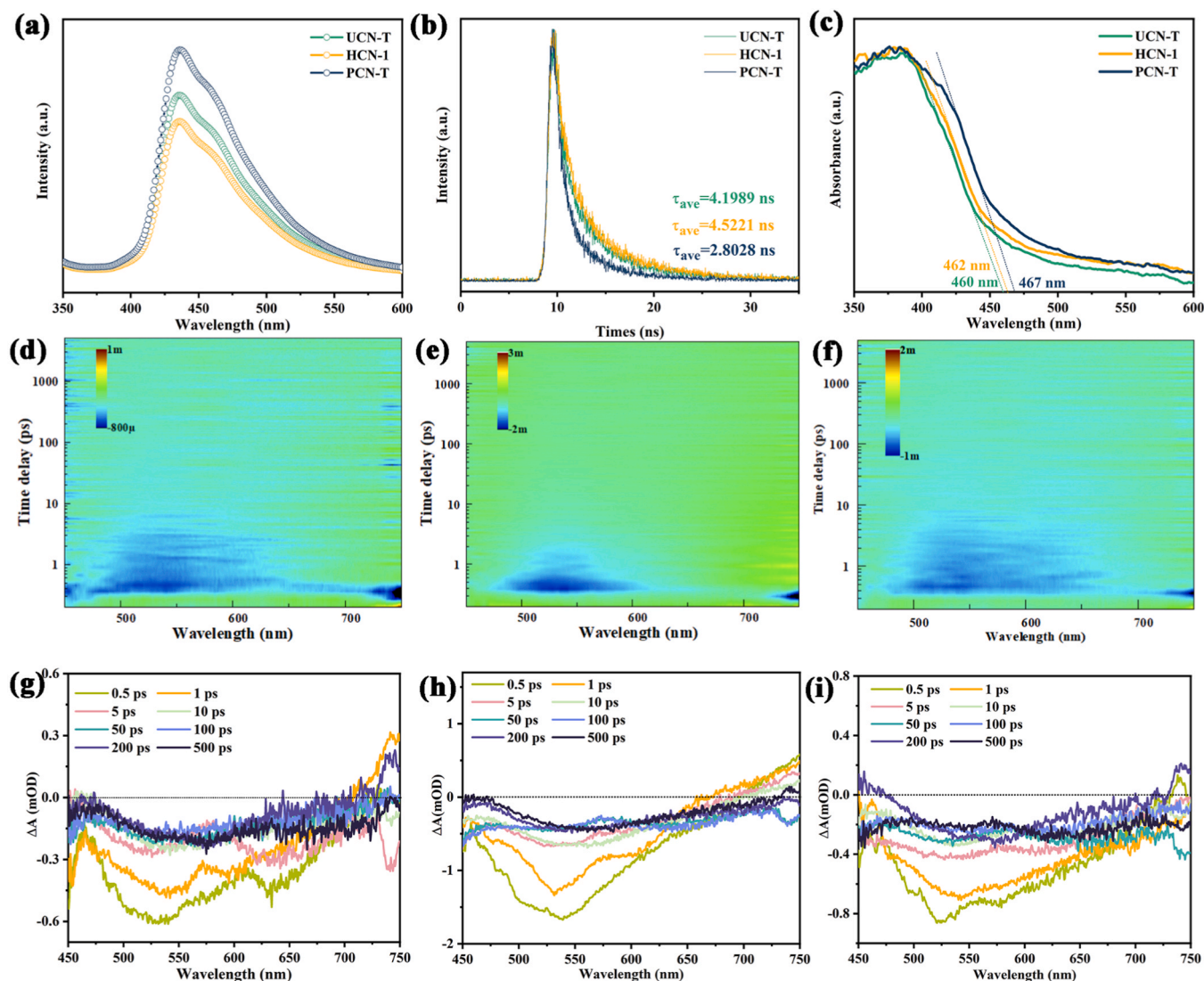
Fig. 2. (a) PL spectra, (b) transient fluorescence spectra and (c) UV–vis spectra of UCN-T, HCN-1 and PCN-T. Pseudocolor fs-TAS curves of (d) UCN-T, (e) HCN-1 and (f) PCN-T. Fs-TA spectra at different delay times of (g) UCN-T, (h) HCN-1 and (i) PCN-T.

coupling effect between UCN and PCN, which may construct a charge transfer channel, causing a shift in the valence and conduction band positions of HCN-1.

Fs-TAS was conducted to further study the transport dynamics of charge carriers. The transient absorbance color maps and fs-TAS were performed under a 360 nm/60 μW excitation in deionized water (Fig. 2d-i). It is reported that the typical negative peak is attributed to ground-state bleaching (GSB), whereas the positive peak aligns with excited-state absorption (ESA) [34,35]. Nevertheless, there is almost no positive signal in all transient absorbance color maps, which is associated with the state-filling signal of the neutral singlet exciton state (electron and hole) [36]. Compared with UCN-T and PCN-T (Fig. 2g and i), the signal of HCN-1 exhibits a significantly narrower profile,

indicative of efficient carrier transport dynamics (Fig. 2h). Moreover, the generation of carriers is positively correlated with the GSB intensity [35], which is arranged as HCN-1 > PCN-T > UCN-T. PCN-T is more conducive to generating charge carriers compared with UCN-T, which can be attributed to the lower band-gap energy (E_g) of PCN-T (2.64 eV) compared with that of UCN-T (2.71 eV) based on the Kubelka–Munk function (Fig. S9). The minor E_g for PCN-T necessitates lower energy for carrier excitation, which possesses unique advantages in the generation of excited charge carriers. It is worth noting that HCN-1 exhibits the highest generation of carriers owing to the optimized band structure through the construction of the homojunction.

To identify the trapping states of charge carriers, the kinetic decay at 520 nm was performed (Fig. S10), and the kinetic fitting results are
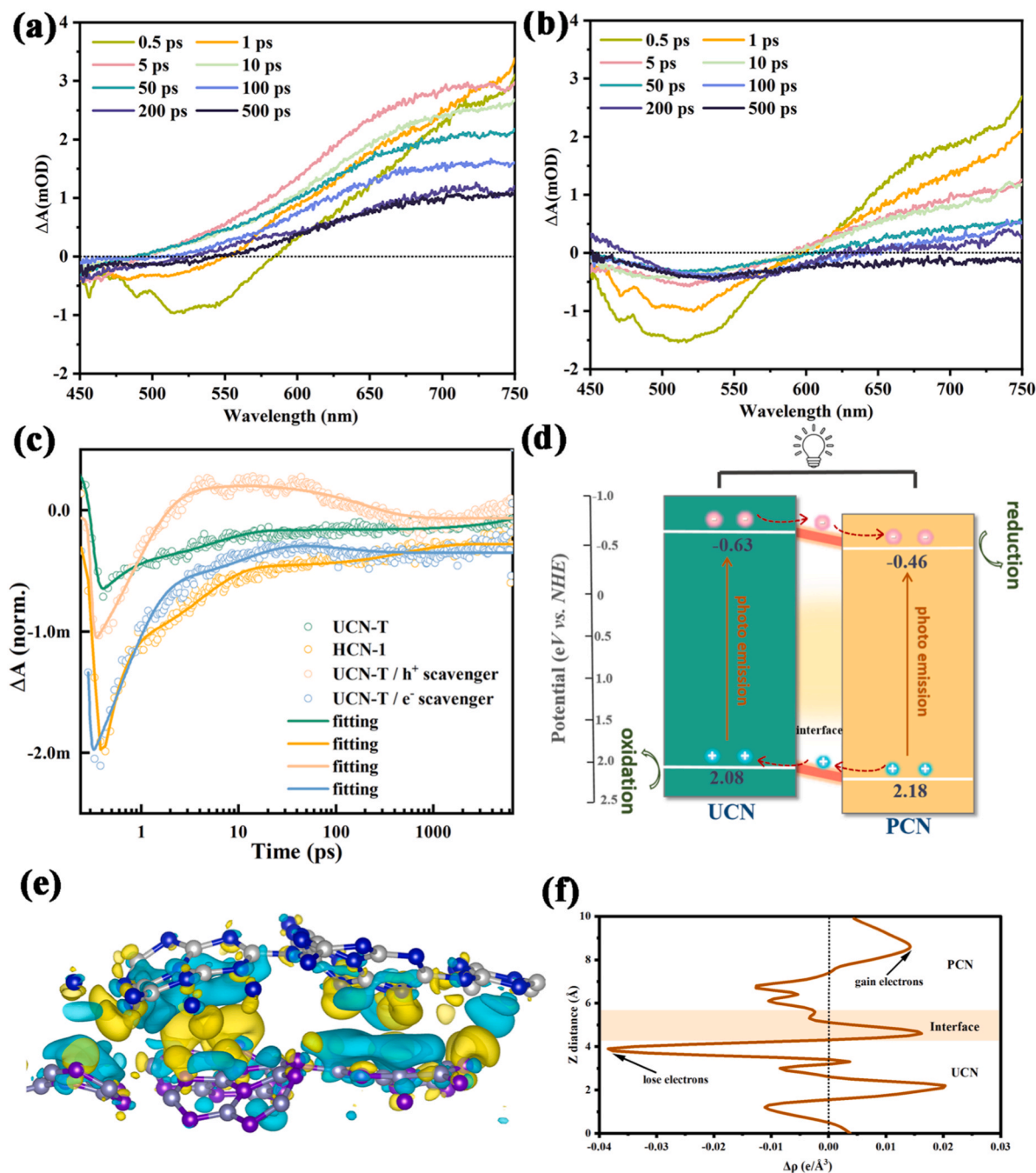

Fig. 3. Fs-TA spectra at different delay times of (a) UCN-T/h⁺ scavenger and (b) UCN-T/e⁻ scavenger. (c) The kinetic decay and fitting curves at 520 nm of UCN-T, HCN-1, UCN-T/h⁺ scavenger and UCN-T/e⁻ scavenger. (d) The charge transfer scheme of the homojunction. (e) The differential charge density and (f) planar averaged charge density difference of HCN-1.

shown in Table S2. For UCN-T, τ_1 and τ_2 are 0.3 ps (26%) and 5.5 ps (28%), respectively, which represent the trapping of charge carriers in short-distance (ST) and long-distance (LT) trap states [37,38]. These charge carriers, confined within shallow traps, are prone to transfer towards the surface and actively engage in subsequent reactions. The ultralong component of τ_3 ($\sim$29758 ps) represents the capture of charge carriers in the deep trap states, which would recombine ultimately. The large proportion of τ_3 (46%) indicates a severe charge carrier recombination of non-geminate electron-hole pairs. In terms of PCN-T, the lifetime of τ_3 is reduced to 8602 ps. However, the recombination ratio of charge carriers still occupies 29%. For HCN-1, the ultralong component (> 1 ns) is not detected, indicating the significantly suppressed recombination efficiency of charge carriers. As compared with UCN-T and PCN-T, the shortest lifetime of τ_1, τ_2 and their largest proportions of HCN-1 demonstrate the shallower trap and more trapped excitons, which could infer that there might be an additional pathway for electron transfer because of the homojunction [39].

To investigate the charge transfer pathway of the constructed homojunction, we introduce 10% triethanolamine as the hole quencher and 10 mM AgNO$_3$ as the electron quencher. The transient absorbance color maps and fs-TAS curves are exhibited in Fig. 3a-b and Fig. S11a-b. A more pronounced GSB signal enhancement is observed for UCN-T/e$^-$ scavenger, which provides compelling evidence for the ability of

electron scavenger to facilitate charge carrier generation profoundly. The kinetic fitting plots and results at 520 nm are shown in Fig. 3c and Table S3. It is observed that no ultralong component for UCN-T/h$^+$ scavenger and UCN-T/e$^-$ scavenger, indicating the significantly restrained recombination efficiency of UCN-T in the presence of scavengers. The comparison of the kinetic decay and fitting curves of UCN-T, HCN-1, UCN-T/h$^+$ scavenger and UCN-T/e$^-$ scavenger is shown in Fig. 3c. The plot of HCN-1 is obviously closer to UCN-T/e$^-$ scavenger, leading to the inference that an additional transport channel is established by PCN acting as an electron scavenger in the homojunction. The effective delivery of electrons from UCN to PCN could remarkably enhance the transport efficiency and reduce the recombination rate of charge carriers.

The flat-band potentials (E_{fb}) are -0.63 and -0.46 eV for UCN-T and PCN-T (Fig. S12). For n-type semiconductors, the E_{fb} is approximately equal to the conduction band potentials (E_{CB}) [40]. Thus, the valence band energy (E_{VB}) can be confirmed according to the equation of $E_{VB} = E_{CB} + E_g$, which are 2.08 and 2.18 eV for UCN-T and PCN-T. The electron configuration of the HCN-1 homojunction is depicted in Fig. 3d, which is conform to typical type-II charge transfer channel. During the photocatalytic process, free charge carriers would be excited and transferred to the surface and interface of UCN and PCN. Because of the potential difference and the closely contacted interface, electrons would rapidly
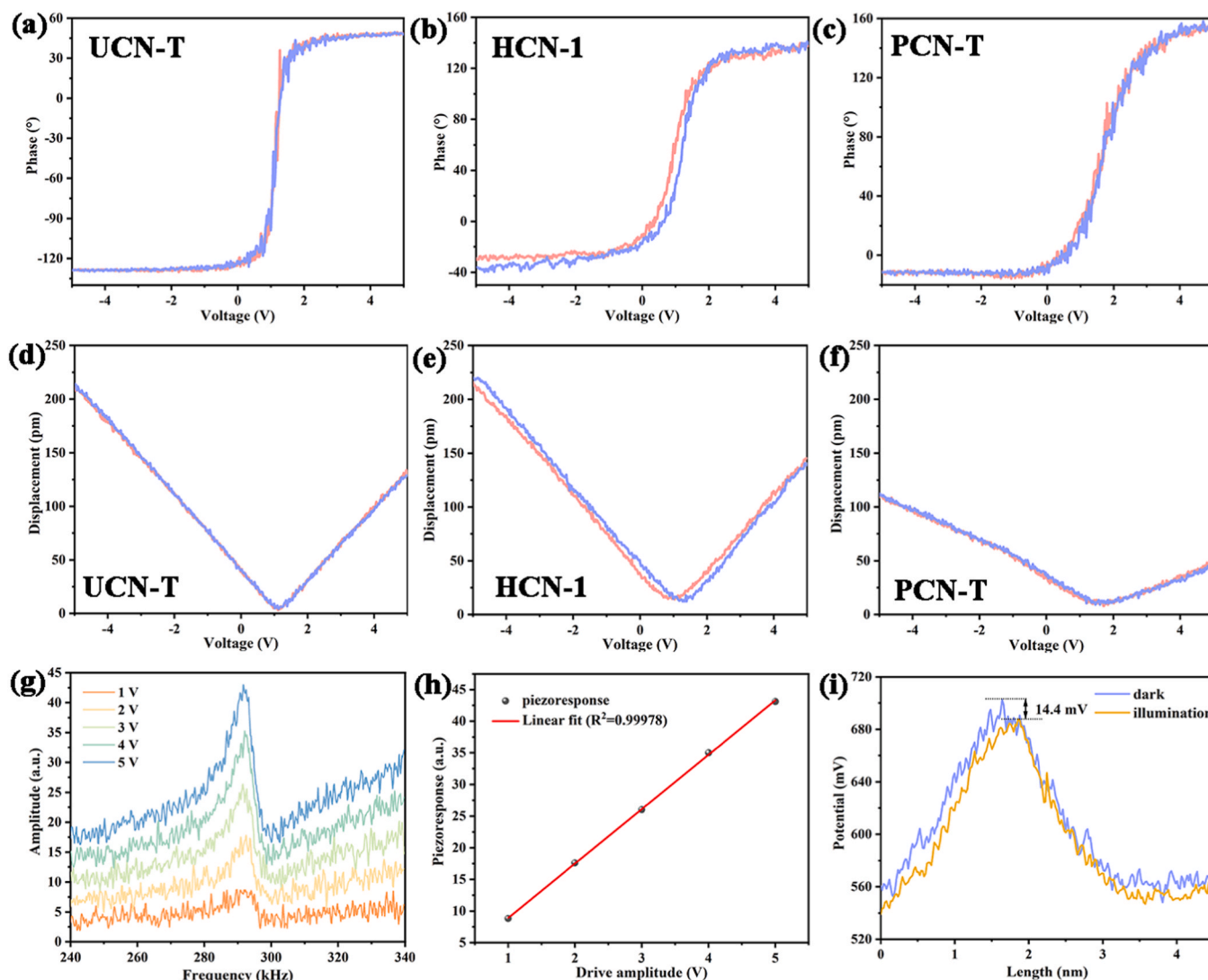

Fig. 4. The phase-voltage of (a) UCN-T, (b) HCN-1 and (c) PCN-T. The displacement–voltage curve of (d) UCN-T, (e) HCN-1 and (f) PCN-T. (g) Resonant peaks and (h) its linear correlation for HCN-1 at the applied voltages of 1–5 V. (i) The surface potential of HCN-1 measured in the dark and under illumination.

transfer from UCN to PCN and holes migrate reversely, therefore distinctly decreasing the recombination efficiency as well as improving the migration efficiency of charge carriers. From the structural optimization model of HCN-1 (Fig. S13), it can be discerned that upon the presence of N vacancy, the two neighboring C atoms are bonded to form a five-membered ring. The charge density difference of HCN-1 is shown in Fig. 3e, where the yellow and blue regions denote electron accumulation and depletion, respectively. Notably, a charge density rearrangement occurs between PCN and UCN, facilitating interlayer electronic charge transfer. In order to further investigate the transfer direction of the charge, the plane-averaged charge density difference is computed and depicted in Fig. 3f. It is revealed that electron loss tends to occur on UCN, while electrons are prone to accumulate on PCN. Consequently, the electron transfer in HCN-1 takes place from UCN to PCN, which corroborating the charge transfer scheme depicted in Fig. 3d.

The piezoelectric property of the samples was analyzed by PFM (Fig. 4a-f). When employing a ramp voltage loop from −5–5 V, the phase reversal of HCN-1 closes to 141°, suggesting an outstanding piezoelectric property of HCN-1 nanosheets (Fig. 4b). Meanwhile, the butterfly

curve of HCN-1 displays the maximum displacement of 220.1 pm, representing their piezoelectric property as expected (Fig. 4e). The formation of piezoelectric polarization is attributed to the presence of positive and negative bound charges on opposite surfaces when the homojunction undergoes deformation under the stress of external forces. However, no phase reversal or butterfly curve is observed for UCN-T and PCN-T, indicating their non-piezoelectricity because of the centrosymmetric structure (Fig. 4a, c, d and f). To further examine the piezoelectric feature of HCN-1, the resonant peaks and the linear correlation between the applied voltage and the amplitude of the displacement for HCN-1 were conducted (Fig. 4g and h). The obvious resonant peaks appear at 291.9 kHz reflected by the piezoelectric vibration, whose peak intensities are linear correlation with the excitation voltage ranging from 1 V to 5 V. KPFM was carried out for HCN-1 under dark environment and light irradiation. As exhibited in Fig. 4i and Fig. S14, the surface voltage is remarkably strong when the material is stressed by the probe tip under dark. However, under light illumination, the surface voltage decreases by 14.4 mV, which is affiliated with the generation of PEF and the dipoles in response to light exposure [19]. The piezo-induced polarization charges can be partially screened by photogenerated electrons
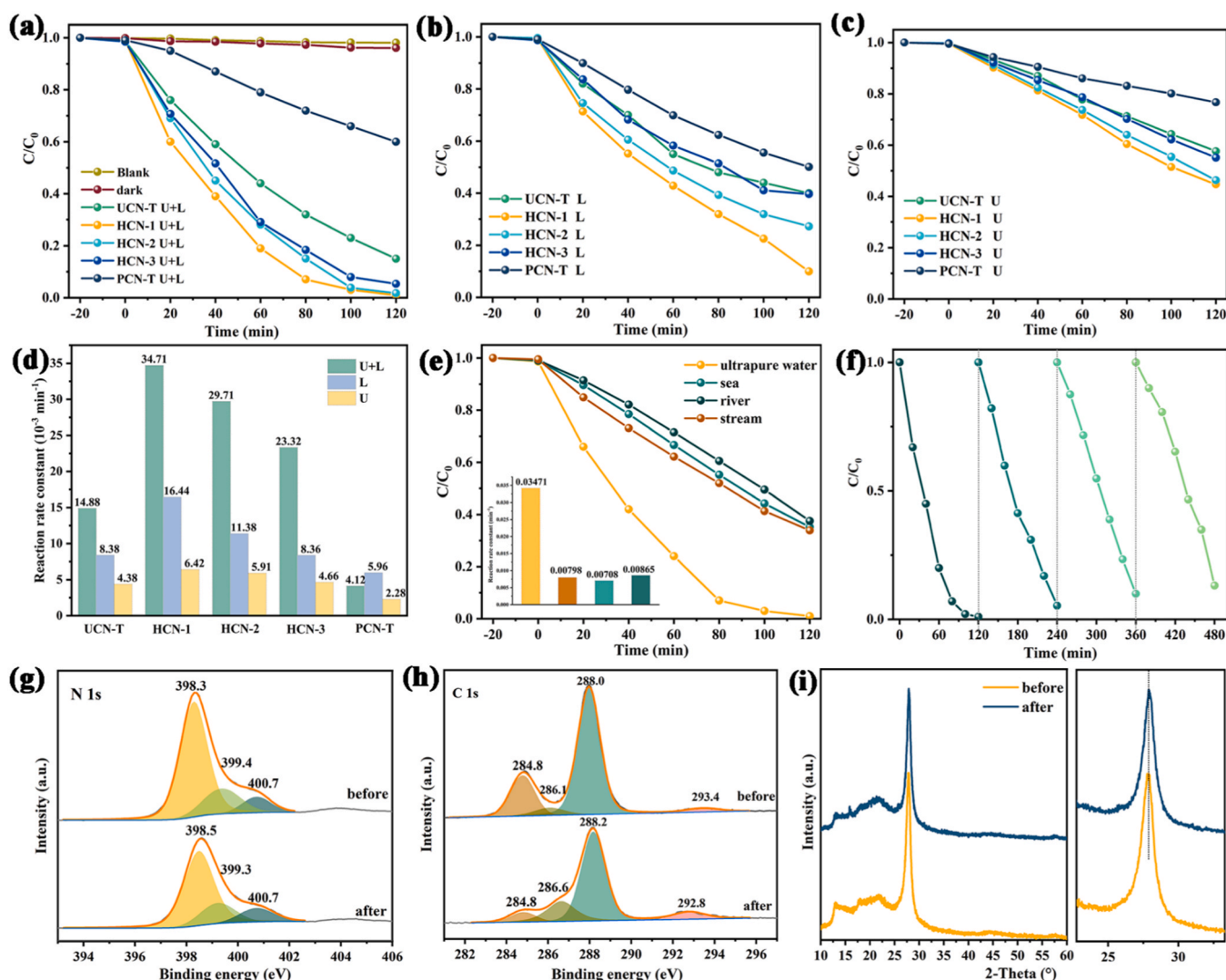
Fig. 5. (a) The photo-piezocatalytic, (b) photocatalyitc and (c) piezocatalytic RhB degradation for UCN-T, HCN-x and PCN-T. (d) The reaction rate constants under light and/or ultrasonic treatment. (e) The photo-piezocatalytic RhB degradation and its reaction rate constants (inserted) of HCN-1 in different water source (Ultrapure water, obtained from laboratory; seawater, obtained from the Bohai Sea; River water, obtained from Xiangjiang River; Stream water, obtained from Pingjiang river). (f) The cycling experiments of HCN-1. The XPS peaks of (g) N 1 s and (h) C 1 s before and after the cycling. (i) The XRD patterns and the enlarged (002) peaks of HCN-1 before and after the cycling.

and holes, evidencing that the PEF is formed in HCN-1 homojunction, while enhancing the separation of photo-induced charge carriers and improving photocatalytic performance.

3.3. Photo-catalytic performances

The photo-piezocatalytic performance is estimated by the degradation of RhB under visible light and ultrasonic (Fig. 5a). The initial concentration of RhB is prescribed as 25 mg L^{-1} (100 mL), which is higher than most other relevant reports. Without adding the catalyst or external stimulation, the degradation efficiency of RhB is only 1.9% after 2 h. Even in the presence of the catalyst, the degradation efficiency is merely 3.9%, which can be ignored for the evaluation. The photo-piezocatalytic RhB degradation efficiency of HCN-x far precedes that of UCN-T and PCN-T, especially for HCN-1 with the degradation efficiency of 99.0% in 2 h (Fig. 5a). The photo-piezocatalytic performance of the homojunction is superior to that of monomer, which is attributed to that the generated PEF in the homojunction allows the migration of photo-stimulated carriers along the piezoelectric polarization [6]. Compared with photocatalytic or piezocatalytic degradation efficiency (Fig. 5b and c), the supreme degradation efficiency is observed on photo-piezocatalysis. According to the higher efficiency of photo-catalysis than that of piezocatalysis, it is reasonable to infer that the light-stimulated charge carriers play the leading role in the superior photo-piezocatalytic performance, and the piezo-stimulated charge carriers serve as the booster. The inner reason for the highest photo-piezocatalytic performance is affiliated with the synergistic effect between the rapid carrier transfer pathways established by the type-II homojunction and the piezoelectric response induced by the non-centrosymmetric structure. It should be noted that piezocatalysis under ultrasonic vibration also demonstrates the phenomenon of sono-chemical catalysis. Despite the confirmation from PFM results that UCN-T and PCN-T do not exhibit piezoelectric response, their performance in degradation is still evident due to the sonocatalytic effect induced by the multifaceted interactions of ultrasonic waves [41].

The estimated reaction rate constants (k) of all samples are exhibited in Fig. 5d and Fig. S15. A superior performance of HCN-1 is observed than that of HCN-2 and HCN-3, which reaches 0.03471 min^{-1} after 2 h photo-piezocatalytic degradation. Even proceeding with individual photo or piezo stimulation, the RhB removal rate of HCN-1 still surpasses that of HCN-2 and HCN-3. It is observed that the catalytic performance of PCN-T is relatively lower than that of UCN-T. Therefore, the excessive ratio of PCN in the homojunction has a detrimental impact on the overall performance, and the proportion of UCN and PCN in the fabrication of the homojunction should be elaborately regulated. The photo-piezocatalytic performance of HCN-1 in four different water sources was assessed (Fig. 5e). The degradation efficiencies processed with seawater, river water and stream water are 64.8%, 62.5% and 66.1%, respectively, significantly lower than that of ultrapure water with the efficiency of 99.0%. This is affiliated with the complex metal ions and organic matter in the natural water source [42]. Significantly, among the most reported literature, the RhB reaction rate constant of HCN-1 for photo-piezocatalysis exhibits a superior performance, indicating a great potential for applications (Fig. S16). Except for evaluating the degradation effect of color pollutants, tetracycline hydrochloride (TC-HCl) was adopted in the same system (Fig. S17). A superior degradation performance of 74.03% in 1 h is obtained for HCN-1 under light and ultrasound, which surpasses the performance under individual external stimulation. This implies an extensive application potential of HCN-1 for different pollutants under the stress of photo-piezocatalysis.

The degradation efficiency of HCN-1 decreases slightly from 99.0% to 86.9% in four cycles, which manifests that the catalytic performance is relatively stable during the process of photo-piezocatalysis (Fig. 5f). The morphology of the used HCN-1 is shown in Fig. S18, which still exhibits homojunction structure with PCN tiled on UCN. Moreover, a delicate change in the movement of N 1 s is observed before and after

cycling (Fig. 5g). For C 1 s peak, the N=C-N peak located at 286.1 eV becomes stronger and shifts to 286.6 eV after the catalytic reaction, indicating the partial fragmentation of the 3-s-triazine ring within the g-C$_3$N$_4$ structure during the ultrasonic process (Fig. 5h). In addition, the peak at 293.4 eV, associated with the π-π conjugation network, exhibits enhanced intensity and a blue shift to 292.8 eV after the reaction, proving that the ultrasonic treatment during the reaction slightly weakened the interlayer coupling effect within the HCN-1. The XRD patterns of HCN-1 before and after four cycles reveal that no apparent shift is observed for the (002) peaks. This indicates that the surface coupling stable perseveres, despite the attenuation over prolonged ultrasonication (Fig. 5i).

The photo-piezocatalytic H$_2$O$_2$ production performance was recorded in ultrapure water and 10% isopropanol. Because of the preferable photo-piezocatalytic RhB degradation of HCN-1, it was selected to represent the homojunction to participate in the following experiment. Before the reaction, the concentration-absorbance standard curve of H$_2$O$_2$ was performed (Fig. S19). In Fig. 6a, the H$_2$O$_2$ production of HCN-1 without photo and piezo is only 13.5 μmol in 1 h, indicating the limited performance in the absence of external stimulation. HCN-1 exhibits a preferable H$_2$O$_2$ production of 635.5 μmol in 1 h under the stimulation of light and ultrasound, which is significantly higher than that of UCN-T and PCN-T. In addition, the H$_2$O$_2$ production of HCN-1 is 432.9 μmol and 290.0 μmol for photocatalysis and piezocatalysis, respectively (Fig. S20a and b). Specially, the piezocatalytic performance of pure water is 35.4 μmol in 1 h, demonstrating that the influence of the ultrasound is low on the production of H$_2$O$_2$. By comparison, it becomes evident that the H$_2$O$_2$ production follows the order of photo-piezocatalysis > photocatalysis > piezocatalysis. This further supports the notion that the light irradiation plays a primary role in the photo-piezocatalytic process, while piezoelectricity acts as an essential auxiliary booster. The PEF could significantly enhance the transfer rate of the light-excited charge carrier, thus resulting in the promoted photo-piezocatalytic H$_2$O$_2$ production for the homojunction [43]. The effect of pH varying from 3 to 10 on the production of H$_2$O$_2$ was conducted (Fig. 6b). As expected, the optimum H$_2$O$_2$ production of 672.6 μM in 1 h is obtained at pH 3, which is ascribed to the fact that more protons are provided in acidic environments. It also displays a competitive property for H$_2$O$_2$ production as compared with other reported g-C$_3$N$_4$ based catalysis. (Fig. S21). After four cycles of reaction, the H$_2$O$_2$ amount only decreases by 6.95%, which exactly manifests the stable catalytic performance of HCN-1 (Fig. 6c).

3.4. Analysis of the reaction mechanism

Exploring the active species involved in the photo-piezocatalysis process plays a crucial role in RhB degradation. During the process of photo-piezocatalysis of HCN-1, butanol (BuOH, 100 mM), ethyl-enediaminetetraacetic acid disodium salt (EDTA-2Na, 2 mM), benzo-quinone (p-BQ, 5 mM) and L-Tryptophan (L-trp, 2 mM) serve as the quencher for •OH, h$^+$, •O$_2^-$, and ^{1}O$_2$, respectively. In Fig. 6d, the degradation efficiencies of RhB are 98.3%, 78.0%, 60.9% and 4.7%, separately, with the addition of BuOH, EDTA-2Na, p-BQ and L-trp. Thus, the reactive substances contribution in this system are arranged as ^{1}O$_2$ > •O$_2^-$ > h$^+$ > •OH. In the presence of •OH quencher, the degradation efficiency is approximate to that of no quencher added HCN-1 (98.3%), indicating almost no devotion of •OH for RhB degradation. When the quencher of ^{1}O$_2$ is added, the almost wholly suppressed degradation efficiency demonstrates the indispensable role of ^{1}O$_2$ in RhB degradation as the reaction oxygen species (ROS) [44]. It may be attributed to the fact that ^{1}O$_2$ would selectively attack electron–rich sites of organic pollutants, thereby breaking the carbon chains of RhB [45,46]. In the presence of •O$_2^-$ and h$^+$ quenchers, the degradation efficiencies are decreased, which indicates that •O$_2^-$ and h$^+$ are involved in the RhB degradation procedure. The electron spin resonance spectra (ESR) were performed for HCN-1. In the dark environment, there is no peak of active
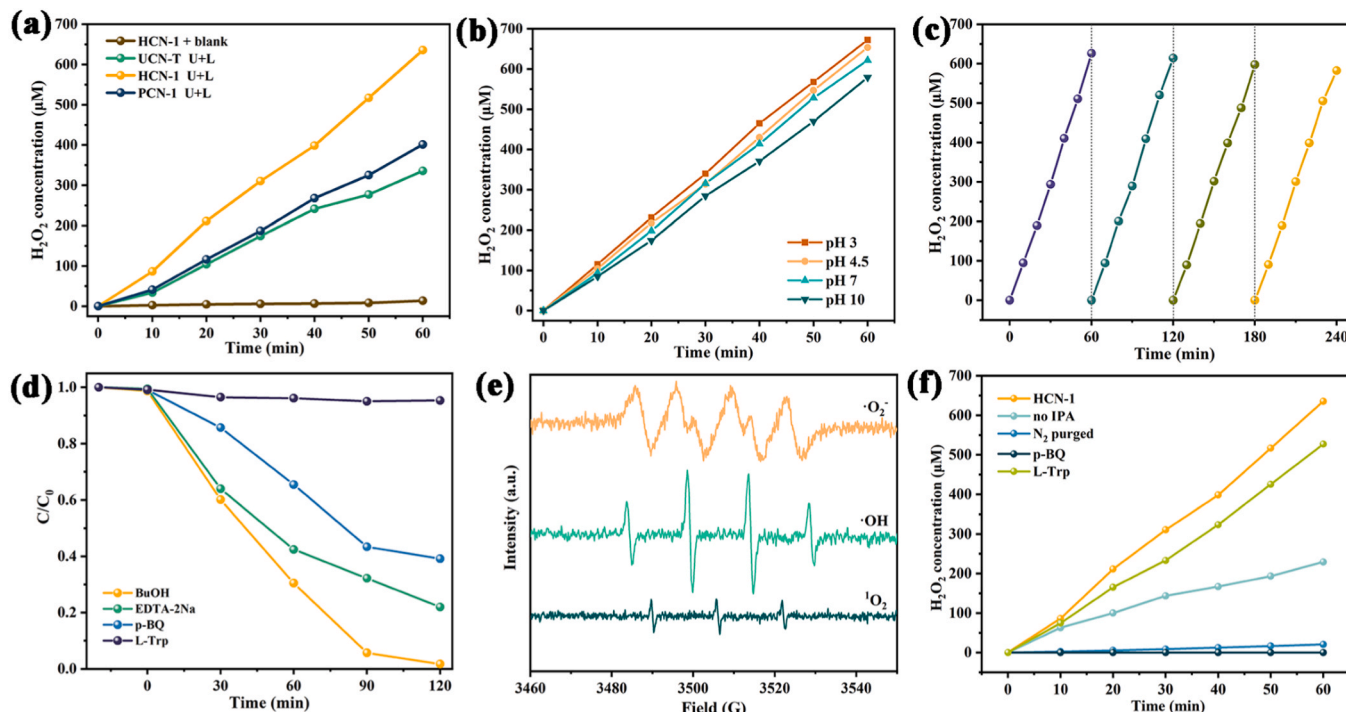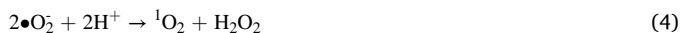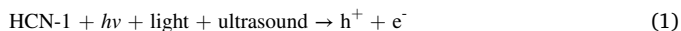
Fig. 6. (a) The photo-piezocatalytic H_2O_2 production. (b) The effect of initial pH for H_2O_2 production. (c) Cycling experiments of HCN-1 for photo-piezocatalytic H_2O_2 production. (d) The RhB degradation efficiency of HCN-1 with different quenching agent. (e) The ESR spectra of $\bullet O_2^-$, $\bullet OH$ and $^1O_2$ under light. (f) The H_2O_2 amount of HCN-1 under different condition.

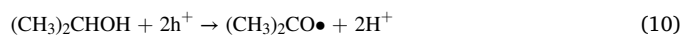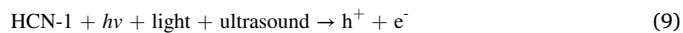species observed (Fig. S22). However, after 10 minutes of light and ul-trasound exposure, the characteristic peaks of $^1O_2$, $\bullet OH$, and $\bullet O_2^-$ are detected, suggesting the formation of these three active species in the photo-piezocatalytic process (Fig. 6e). Based on the data above, the degradation process of RhB could be elucidated as the following equa-tions [47]:

$$HCN\text{-}1 + h\nu + light + ultrasound \rightarrow h^+ + e^- \tag{1}$$

$$2H_2O + 4h^+ \rightarrow O_2 + 4H^+ \tag{2}$$

$$e^- + O_2 \rightarrow \bullet O_2^- \tag{3}$$

$$2\bullet O_2^- + 2H^+ \rightarrow {}^1O_2 + H_2O_2 \tag{4}$$

$$H_2O_2 + e^- \rightarrow \bullet OH + OH^- \tag{5}$$

$$\bullet O_2^- + h^+ \rightarrow {}^1O_2 \tag{6}$$

$$O_2 \rightarrow {}^1O_2 \tag{7}$$

$$\bullet O_2^- + {}^1O_2 + h^+ + H_2O_2 + RhB \rightarrow Degradation\ products \tag{8}$$

Under the influence of ultrasound and light radiation, photo-excited charge carriers are generated. Due to the band gap structure satisfying $O_2/\bullet O_2^-$ (−0.33 eV NHE) and O_2/H_2O_2 (+0.69 eV NHE) [47], O_2 reacts with electrons to initially generate $\bullet O_2^-$ (Eqnation 3), which then com-bines with H^+ to produce H_2O_2 and $^1O_2$ with higher oxidation activity (Eqnation 4). Besides, the accumulation of $\bullet O_2^-$ in HCN-1 increases the probability of their trapping holes from g-C_3N_4 to generate $^1O_2$ (Eqna-tion 6). The indispensable species of $^1O_2$ is a derivative of $\bullet O_2^-$, which is always generated through the process of electron transfer. However, the degradation efficiency of $\bullet O_2^-$ quencher is lower than that of $^1O_2$ quencher. Thus, it is reasonable to deduce that an alternative pathway through energy transfer is provided for the generation of $^1O_2$ (Eqnation 7) [48,49]. As a result, the combined action of $^1O_2$, $\bullet O_2^-$, h^+ and inter-mediate H_2O_2 degrades RhB into CO_2, H_2O and degradation intermediates.

The primary ROS involved in piezo-photocatalytic H_2O_2 production

over HCN-1 was investigated in Fig. 6f. The absence of IPA leads to a decrease in H_2O_2 production, as IPA plays a role in providing the source of hydrogen for the reaction. In the absence of IPA, active species can only react with H_2O to generate H^+, leading to an excessively elevated energy barrier [50]. As N_2 purged into the solution to eliminate the dissolved O_2, the production of H_2O_2 is sharply decreased to 53.2 μmol h^{-1}. It is exactly demonstrated that ROS is generated from oxygen reduction instead of water oxidation. As the quencher of $\bullet O_2^-$, the addition of p-BQ completely inhibits the synthesis of H_2O_2. What's more, the addition of L-trp (the quencher of $^1O_2$) could reduce the H_2O_2 production from 635.5 μmol to 527.1 μmol. These findings indicate the critical involvement of $^1O_2$ and the indispensable role of $\bullet O_2^-$, which are the main ROS in the production of H_2O_2. It suggests that both $\bullet O_2^-$ and $^1O_2$ can generate H_2O_2 through stepwise electron reduction. Therefore, these two reactions compete with each other for the radical species in the composite system, possibly promoting the production of H_2O_2. The following equations could clearly expound the generation process of H_2O_2 [49,51]:

$$HCN\text{-}1 + h\nu + light + ultrasound \rightarrow h^+ + e^- \tag{9}$$

$$(CH_3)_2CHOH + 2h^+ \rightarrow (CH_3)_2CO\bullet + 2H^+ \tag{10}$$

$$2H_2O + 4h^+ \rightarrow O_2 + 4H^+ \tag{11}$$

$$O_2 + 2H^+ + 2e^- \rightarrow H_2O_2 \tag{12}$$

$$e^- + O_2 \rightarrow \bullet O_2^- \tag{13}$$

$$\bullet O_2^- + h^+ \rightarrow {}^1O_2 \tag{14}$$

$$\bullet O_2^- + 2H^+ + e^- \rightarrow H_2O_2 \tag{15}$$

$$O_2 \rightarrow {}^1O_2 \tag{16}$$

$$^1O_2 + 2H^+ + 2e^- \rightarrow H_2O_2 \tag{17}$$

The charge carriers are generated under the stimulation of light and ultrasonic. The holes on the catalyst surface promptly engage in an

oxidative reaction with IPA, yielding H$^+$ and acetone (Eqnation 10). A portion of oxygen can directly react with protons to form H$_2$O$_2$ (Eqnation 12). Another portion of the oxygen is reduced to •O$_2^-$, which then combines with H$^+$ to produce H$_2$O$_2$ (Eqnation 13 and 15). ^{1}O$_2$ can be derived from •O$_2^-$ through electron transfer or synthesized through energy transfer, ultimately combining with protons to generate H$_2$O$_2$ (Eqnation 14, 16 and 17).

By scrutinizing the band structure depicted in Fig. 3d, it can be deduced that the positions of E$_{VB}$ and E$_{CB}$ for HCN-1 satisfy the oxidation-reduction reactions involved in the degradation of RhB and the production of H$_2$O$_2$ at various stages. Notably, within the confines of the semiconductor material, the liberation of free electrons and holes can be thermally activated at ambient temperature. However, it is imperative to acknowledge that at the state of thermal equilibrium, the concentration of free charges decreases to an exceedingly low magnitude (Fig. S23). In the absence of external stimulation to induce charge transfer, it is hard to observe significant catalytic reactions. When the system is subjected to ultrasonic vibration, extremely dense bubbles will be generated in the solution. The collapse of the bubbles will create high local pressure (>100 Mpa) as well as forming local hotspots [52], which in turn results in the emergence of local strain and polarized charges in the homojunction [53]. Under the influence of PEF, free electrons and holes migrate to the opposite directions, thereby promoting the efficiency of bulk separation in HCN-1 homojunction. Meanwhile, the valence band (VB) and conduction band (CB) are tilted by the piezoelectric potential due to the sustained mechanical force, and the slope is

correlated with the piezoelectric potential [54]. As shown in Fig. 7a, when the polarization direction (P$_{PZ}$) points from UCN to PCN, the CB decreases along the P$_{PZ}$, while the VB increases along the P$_{PZ}$. Both electrons and holes at CB and VB prefer to move toward the lower potential. Thus, the type-II charge transfer channel is established, in which the polar-generated electrons driven by the PEF migrate from UCN to PCN at the CB position, while the polar-generated holes transfer oppositely from PCN to UCN at the VB position. When the P$_{PZ}$ points from PCN to UCN (Fig. 7b), the direction of band tilting is reversed. The electrons at CB of PCN tend to recombine with the holes at VB of UCN. This arrangement allows the electrons remaining in the CB of UCN to facilitate the reduction reaction, while the holes remaining at VB of PCN assist in the oxidation reaction. The establishment of Z-scheme charge transfer channel promotes the recombination of useless electrons and holes through coulombic attraction. However, merely relying on piezoelectric polarization is inadequate to effectively induce the production of a significant number of charge carriers. Furthermore, the occurrence of transient free charge recombination, resulting from thermal excitation, further hampers the overall piezoelectric catalytic performance.

In particular, for the coupled photo-piezocatalytic effect on the homojunction, the reaction system undergoes dual stimulation for visible light radiation and mechanical squeezing. By virtue of the PEF, the photo-excited and polar-generated charge carriers could efficiently separate and migrate along the opposite direction. Therefore, the highly suppressed recombination efficiency is achieved, facilitating a larger
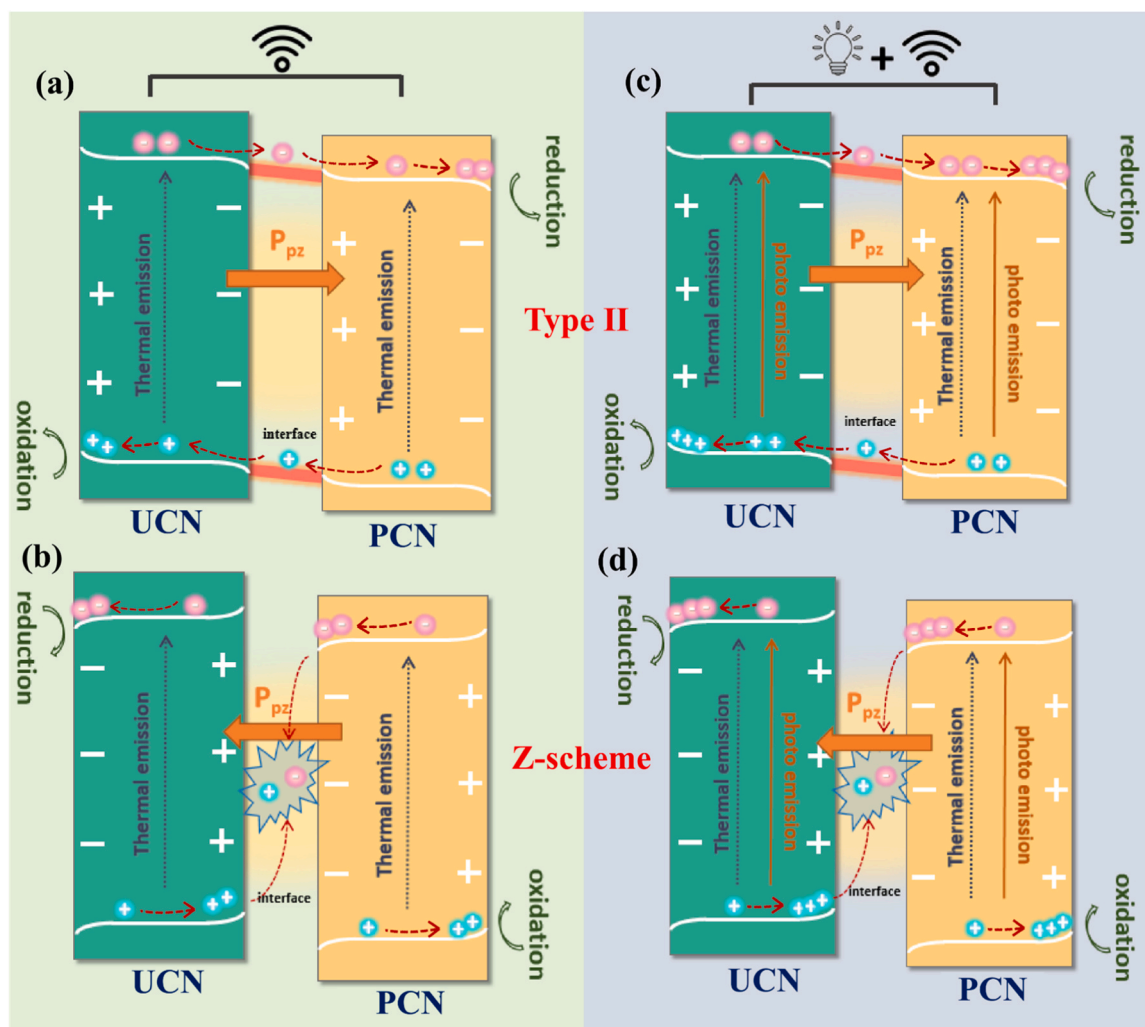

Fig. 7. Schematic mechanism of (a, b) the piezocatalytic process and (c, d) photo-piezocatalytic process at different P$_{PZ}$.

number of effective electron-hole pairs to migrate to the CB and VB position. As the P_{PZ} points from UCN to PCN (Fig. 7c), the direction of PEF is the same as IEF and the type-II charge transfer channel is constructed. The effect of the dual electric field causes an accelerated interface transfer rate of electrons to the CB of PCN, where the reactive intermediates of $\bullet O_2^-$ or H_2O_2 are generated. At the same time, the efficient interface transfer of holes at the VB of UCN participates in the reduction reactions of $\bullet O_2^-$ / $^1O_2$. These intermediates are potent inducers for RhB degradation and H_2O_2 production. As the P_{PZ} points from PCN to UCN (Fig. 7d), a Z-scheme charge transfer channel is naturally formed, allowing a considerable amount of electrons accumulated at the CB of UCN to undergo reduction reactions, while the holes congregated at VB of PCN promote oxidation reactions. In summary, both types of charge transfer mechanisms contribute significantly to the increased catalytic activity of HCN-1. Especially, the direction and the value of PEF are not constant. Piezoelectric polarization increases with bubble formation and growth, subsequently decreases to the equilibrium when it collapses [55]. Upon finishing this period, the polarization direction may change in response to environmental variation. Thus, in the process of photo-piezocatalysis, the charge transfer pathway undergoes transformation between type-II and Z-scheme mechanisms.

4. Conclusion

In summary, a novel heteroatom-free UCN/PCN homojunction is constructed through the surface coupling effect. The matched band structure allows for the construction of type-II homojunction, which provides an additional transfer channel for photo-induced charge carriers. Additionally, the non-centrosymmetric structure of the homojunction facilitates the generation of the polarized electric field, which acts as a powerful booster for the spatial separation and efficient migration of the photo-excited carriers. Based on data analysis, a switching charge transfer dynamics between the type-II and Z-scheme mechanisms is proposed. As a result, the reaction rate constant reaches $0.03471 \, min^{-1}$ at a high RhB concentration of $25 \, mg \, L^{-1}$, and the photo-piezocatalytic H_2O_2 production can achieve 672.6 µmol in 1 h at pH 3. This research provides a new avenue to design a facile and highly efficient photo-piezocatalyst for mitigating energy crises and environmental pollution.

CRediT authorship contribution statement

Yi Zhang: Data curation. **Jiaxin Tong:** Validation, Investigation. **Huanhuan Zhai:** Writing – original draft, Methodology, Investigation. **Hongqin Liu:** Resources, Data curation. **Pengfei Tan:** Funding acquisition, Data curation. **Jun Pan:** Supervision, Project administration, Funding acquisition, Formal analysis. **Wenna Du:** Resources, Methodology. **Hanxiao Liao:** Supervision, Methodology. **Xinfeng Liu:** Supervision.

Author contibutions

J. Pan conceived and directed this work. H.X. Liao and W.N. Du supervised the experiments. H.H. Zhai fabricated the samples. H.H. Zhai did the characterizations and experiments with assistance from H.Q. Liu, Y. Zhang, J.X. Tong. H.H. Zhai and J. Pan wrote the paper. P.F. Tan and X.F. Liu guided the writing. All coauthors discussed the results and helped in organizing the manuscript.

Declaration of Competing Interest

The authors declare that they have no known competing financial interests or personal relationships that could have appeared to influence the work reported in this paper.

Data availability

Data will be made available on request.

Appendix A. Supporting information

Supplementary data associated with this article can be found in the online version at doi:10.1016/j.apcatb.2024.123909.

References

[1] G.Z.S. Ling, S.F. Ng, W.J. Ong, Tailor-engineered 2D cocatalysts: harnessing electron-hole redox center of 2D g-C_3N_4 photocatalysts toward solar-to-chemical conversion and environmental purification, Adv. Funct. Mater. 32 (2022) 211187.

[2] H. Li, S.T. Sun, H.D. Ji, W. Liu, Z.R. Shen, Enhanced activation of molecular oxygen and degradation of tetracycline over Cu-S_4 atomic clusters, Appl. Catal. B 272 (2020) 118966.

[3] J.X. Tong, H.H. Zhai, S.G. Zhao, L.S. Song, G.Z. Wang, N.N. Feng, P.F. Tan, J.P. Xie, J. Pan, Visible light-driven sliver-modified titanium dioxide / bismuth molybdenum oxide with rapid interfacial charge-transfer for dual highly efficient photocatalytic degradation and disinfection, J. Colloid Interf. Sci. 653 (2024) 285–295.

[4] J. Wang, T. Liao, Z.Z. Wei, J.T. Sun, J.J. Guo, Z.Q. Sun, Heteroatom-doping of non-noble metal-based catalysts for electrocatalytic hydrogen evolution: an electronic structure tuning strategy, Small Methods 5 (2021) 2000988.

[5] H.X. Liao, G.H. Ni, P.F. Tan, K. Liu, X.Z. Liu, H.L. Liu, K.J. Chen, X.S. Zheng, M. Liu, J. Pan, Oxyanion engineering suppressed iron segregation in nickel-iron catalysts toward stable water oxidation, Adv. Mater. 35 (2023) 2300347.

[6] Z. Liang, C.F. Yan, S. Rtimi, J. Bandara, Piezoelectric materials for catalytic/ photocatalytic removal of pollutants: recent advances and outlook, Appl. Catal. B 241 (2019) 256–269.

[7] S.Y. Lan, J.X. Feng, Y. Xiong, S.H. Tian, S.W. Liu, L.J. Kong, Performance and mechanism of piezo-catalytic degradation of 4-chlorophenol: finding of effective piezo-dechlorination, Environ. Sci. Technol. 51 (2017) 6560–6569.

[8] M.Y. Wang, B. Wang, F. Huang, Z.Q. Lin, Enabling PIEZOpotential in PIEZOelectric semiconductors for enhanced catalytic activities, Angew. Chem. Int Ed. 58 (2019) 7526–7536.

[9] Z.L. Wang, Piezopotential gated nanowire devices: piezotronics and piezo-phototronics, Nano Today 5 (2010) 540–552.

[10] C.F. Pan, S.M. Niu, Y. Ding, L. Dong, R.M. Yu, Y. Liu, G. Zhu, Z.L. Wang, Enhanced Cu_2S/CdS coaxial nanowire solar cells by piezo-phototronic effect, Nano Lett. 12 (2012) 3302–3307.

[11] M. Fiebig, T. Lottermoser, D. Meier, M. Trassin, The evolution of multiferroics, Nat. Rev. Mater. 4 (2019), 146-146.

[12] M.Y. Zhang, S.Y. Nie, T. Cheng, Y. Feng, C.C. Zhang, L. Zheng, L. Wu, W.C. Hao, Y. Ding, Enhancing the macroscopic polarization of CdS for piezo-photocatalytic water splitting, Nano Energy 90 (2021) 106635.

[13] X.F. Zhou, S.H. Wu, C.B. Li, F. Yan, H.R. Bai, B. Shen, H.R. Zeng, J.W. Zhai, Piezophototronic effect in enhancing charge carrier separation and transfer in ZnO/$BaTiO_3$ heterostructures for high-efficiency catalytic oxidation, Nano Energy 66 (2019) 104127.

[14] F. Wang, J.T. Zhang, C.C. Jin, X.C. Ke, F.F. Wang, D.M. Liu, Unveiling the effect of crystal facets on piezo-photocatalytic activity of $BiVO_4$, Nano Energy 101 (2022) 107573.

[15] Z.J. Wang, T.C. Hu, H.X. He, Y.M. Fu, X. Zhang, J. Sun, L.L. Xing, B.D. Liu, Y. Zhang, X.Y. Xue, Enhanced H_2 production of TiO_2/ZnO nanowires co-using solar and mechanical energy through piezo-photocatalytic effect, ACS Sustain. Chem. Eng. 6 (2018) 10162–10172.

[16] X.Y. Huang, R. Lei, J. Yuan, F. Gao, C.K. Jiang, W.H. Feng, J.D. Zhuang, P. Liu, Insight into the piezo-photo coupling effect of $PbTiO_3$/CdS composites for piezo-photocatalytic hydrogen production, Appl. Catal. B 282 (2021) 119586.

[17] X.D. Zhao, Q. Liu, X.L. Li, H.M. Ji, Z.R. Shen, Two-dimensional g-C_3N_4 nanosheets-based photo-catalysts for typical sustainable processes, Chin. Chem. Lett. 34 (2023) 108306.

[18] Q. Liu, H. Li, H. Zhang, Z.R. Shen, H.M. Ji, The role of Cs dopants for improved activation of molecular oxygen and degradation of tetracycline over carbon nitride, Chin. Chem. Lett. 33 (2022) 4756–4760.

[19] C. Hu, F. Chen, Y.G. Wang, N. Tian, T.Y. Ma, Y.H. Zhang, H.W. Huang, Exceptional cocatalyst-free photo-enhanced piezocatalytic hydrogen evolution of carbon nitride nanosheets from strong in-plane polarization, Adv. Mater. 33 (2021).

[20] C.C. Liu, W.Q. Ma, J.J. Chen, Z.Y. Mao, D.J. Wang, Synergetic photocatalytic and piezocatalytic degradation of organic pollutants over graphite carbon nitride, J. Mater. Sci. -Mater. El 32 (2021) 25033–25044.

[21] H.T. Vuong, D.V. Nguyen, P.P. Ly, P.D.M. Phan, T.D. Nguyen, D. Tran, P.T. Mai, N. H. Hieu, Defect engineering of porous g-C_3N_4 to add multifunctional groups for enhanced production of H_2O_2 via piezo-photocatalysis, ACS Appl. Nano Mater. 6 (2023) 664–676.

[22] X.J. Guan, S.C. Zong, S.H. Shen, Homojunction photocatalysts for water splitting, Nano Res 15 (2022) 10171–10184.

[23] F.K. Wang, K. Pei, Y. Li, H.Q. Li, T.Y. Zhai, 2D homojunctions for electronics and optoelectronics, Adv. Mater. 33 (2021) 2005303.

[25] T. Xu, Z. Xia, H. Li, P. Niu, S. Wang, L. Li, Constructing crystalline g-C_3N_4/g-$C_3N_{4-x}S_x$ isotype heterostructure for efficient photocatalytic and piezocatalytic performances, Energy Environ. Mater. 6 (2022) e12306.

[24] R.D. Tang, D.X. Gong, Y.Y. Zhou, Y.C. Deng, C.Y. Feng, S. Xiong, Y. Huang, G. W. Peng, L. Li, Unique g-C_3N_4/PDI-g-C_3N_4 homojunction with synergistic piezo-photocatalytic effect for aquatic contaminant control and H_2O_2 generation under visible light, Appl. Catal. B 303 (2022) 120929.

[26] P. Niu, L.L. Zhang, G. Liu, H.M. Cheng, Graphene-like carbon nitride nanosheets for improved photocatalytic activities, Adv. Funct. Mater. 22 (2012) 4763–4770.

[27] H.W. Huang, K. Xiao, N. Tian, F. Dong, T.R. Zhang, X. Du, Y.H. Zhang, Template-free precursor-surface-etching route to porous, thin g-C_3N_4 nanosheets for enhancing photocatalytic reduction and oxidation activity, J. Mater. Chem. A 5 (2017) 17452–17463.

[28] Z.W. Xiong, Z. Wang, M. Murugananthan, Y.R. Zhang, Construction of an in-situ Fenton-like system based on a g-C_3N_4 composite photocatalyst, J. Hazard. Mater. 373 (2019) 565–571.

[29] L. Padmaja, C. Ravikumar, D. Sajan, I.H. Joe, V.S. Jayakumar, G.R. Pettit, O. F. Nielsen, Density functional study on the structural conformations and intramolecular charge transfer from the vibrational spectra of the anticancer drug combretastatin-A2, J. Raman Spectrosc. 40 (2009) 419–428.

[30] H.J. Dong, X.X. Zhang, J.M. Li, P.J. Zhou, S.Y. Yu, N. Song, C.B. Liu, G.B. Che, C. M. Li, Construction of morphology-controlled nonmetal 2D/3D homojunction towards enhancing photocatalytic activity and mechanism insight, Appl. Catal. B 263 (2020) 118270.

[31] C.M. Li, S.Y. Yu, H.N. Che, X.X. Zhang, J. Han, Y.L. Mao, Y. Wang, C.B. Liu, H. J. Dong, Fabrication of Z-scheme heterojunction by anchoring mesoporous gamma-Fe_2O_3 nanospheres on g-C_3N_4 for degrading tetracycline hydrochloride in water, ACS Sustain. Chem. Eng. 6 (2018) 16437–16447.

[32] Z.D. Wei, J.Y. Liu, W.J. Fang, M.Q. Xu, Z. Qin, Z. Jiang, W.F. Shangguan, Photocatalytic hydrogen evolution with simultaneous antibiotic wastewater degradation via the visible-light-responsive bismuth spheres-g-C_3N_4 nanohybrid: waste to energy insight, Chem. Eng. J. 358 (2019) 944–954.

[33] J.J. Jiao, Z.X. Wang, J. Wang, T.T. Yao, Z.L. Chen, C. Chen, L. Sun, X. Zhao, W. L. Fan, g-C_3N_4-based homojunction induced by Ag and P selective doping for improved photocatalytic H2 evolution coupled with tetracycline degradation: type-II versus S-scheme mechanism, Appl. Surf. Sci. 639 (2023) 158260.

[34] R. Godin, Y. Wang, M.A. Zwijnenburg, J.W. Tang, J.R. Durrant, Time-resolved spectroscopic investigation of charge trapping in carbon nitrides photocatalysts for hydrogen generation, J. Am. Chem. Soc. 139 (2017) 5216–5224.

[35] K.L. Corp, C.W. Schlenker, Ultrafast spectroscopy reveals electron-transfer cascade that improves hydrogen evolution with carbon nitride photocatalysts, J. Am. Chem. Soc. 139 (2017) 7904–7912.

[36] J. Huang, B.S. Wang, Z.J. Hao, Z.R. Zhou, Y. Qu, Boosting charge separation and broadening NIR light response over defected WO_3 quantum dots coupled g-C_3N_4 nanosheets for photocatalytic degrading antibiotics, Chem. Eng. J. 416 (2021) 129109.

[37] J.W. Xue, M. Fujitsuka, T. Majima, Shallow trap state-induced efficient electron transfer at the interface of heterojunction photocatalysts: the crucial role of vacancy defects, ACS Appl. Mater. Interfaces 11 (2019) 40860–40867.

[38] P. Singh, K. Gaur, N. Ghorai, T. Goswami, A. Thakur, H.N. Ghosh, Temperature-dependent trap-assisted ultrafast carrier dynamics in amorphous and crystalline In_2Se_3 thin films, Phys. Rev. Appl. 14 (2020) 14087.

[39] X. Xiao, Y. Gao, L. Zhang, J. Zhang, Q. Zhang, Q. Li, H. Bao, J. Zhou, S. Miao, N. Chen, J. Wang, B. Jiang, C. Tian, H. Fu, A promoted charge separation/transfer system from Cu single atoms and C_3N_4 layers for efficient photocatalysis, Adv. Mater. 32 (2020) 2003082.

[40] D. Liu, S. Zhang, J.M. Wang, T.Y. Peng, R.J. Li, Direct Z-scheme 2D/2D photocatalyst based on ultrathin g-C_3N_4 and WO_3 nanosheets for efficient visible-light-driven H_2 generation, ACS Appl. Mater. Interfaces 11 (2019) 27913–27923.

[41] S. Verma, M. Sharma, R. Vaish, Photo-piezocatalysis in electrospun PVDF + WS_2 membrane, Environ. Sci. -Nano 9 (2022) 3885–3899.

[42] R.J. Zheng, J. Li, R.L. Zhu, R.H. Wang, X.Z. Feng, Z.J. Chen, W.F. Wei, D.Z. Yang, H. Chen, Enhanced Cr(VI) reduction on natural chalcopyrite mineral modulated by degradation intermediates of RhB, J. Hazard. Mater. 423 (2022) 127206.

[43] J. Yuan, X.Y. Huang, L.L. Zhang, F. Gao, R. Lei, C.K. Jiang, W.H. Feng, P. Liu, Tuning piezoelectric field for optimizing the coupling effect of piezo-photocatalysis, Appl. Catal. B 278 (2020) 119291.

[44] Z.D. Li, D.F. Liu, Y.X. Zhao, S.R. Li, X.C. Wei, F.S. Meng, W.L. Huang, Z.F. Lei, Singlet oxygen dominated peroxymonosulfate activation by CuO-CeO_2 for organic pollutants degradation: performance and mechanism, Chemosphere 233 (2019) 549–558.

[45] S.K. Chaharsooghi, M. Honarvar, M. Modarres, A multi-stage stochastic programming model for dynamic pricing and lead time decisions in multi-class make-to-order firm, Sci. Iran. 18 (2011) 711–721.

[46] X.Z. Niu, F. Busetti, M. Langsa, J.P. Croué, Roles of singlet oxygen and dissolved organic matter in self-sensitized photo-oxidation of antibiotic norfloxacin under sunlight irradiation, Water Res 106 (2016) 214–222.

[47] J.Q. Zhang, J. Li, X.Y. Liu, Ternary nanocomposite ZnO-g-C_3N_4-Go for enhanced photocatalytic degradation of RhB, Opt. Mater. 119 (2021) 111351.

[48] Q. Li, F.T. Li, Recent advances in molecular oxygen activation via photocatalysis and its application in oxidation reactions, Chem. Eng. J. 421 (2021) 129915.

[49] J.N. Li, J.H. Huang, G.M. Zeng, C.Y. Zhang, H.B. Yu, Q.F. Wan, K.X. Yi, W. Zhang, H.L. Pang, S. Liu, S.Z. Li, W.J. He, Efficient photosynthesis of H_2O_2 via two-electron oxygen reduction reaction by defective g-C_3N_4 with terminal cyano groups and nitrogen vacancies, Chem. Eng. J. 463 (2023) 142512.

[50] J. Luo, Y.N. Liu, C.Z. Fan, L. Tang, S.J. Yang, M.L. Liu, M.E. Wang, C.Y. Feng, X. L. Ouyang, L.L. Wang, L. Xu, J.J. Wang, M. Yan, Direct Attack and indirect transfer mechanisms dominated by reactive oxygen species for photocatalytic H_2O_2 production on g-C_3N_4 possessing nitrogen vacancies, ACS Catal. 11 (2021) 11440–11450.

[51] W.H. Zhang, Y.Y. Peng, Y.J. Yang, L. Zhang, Z.Y. Bian, H. Wang, Bismuth-rich strategy intensifies the molecular oxygen activation and internal electrical field for the photocatalytic degradation of tetracycline hydrochloride, Chem. Eng. J. 430 (2022) 132963.

[52] J.H. Bang, K.S. Suslick, Applications of ultrasound to the synthesis of nanostructured materials, Adv. Mater. 22 (2010) 1039–1059.

[53] G. Tezcanli-Guyer, N.H. Ince, Individual and combined effects of ultrasound, ozone and UV irradiation: a case study with textile dyes, Ultrasonics 42 (2004) 603–609.

[54] S.C. Rai, K. Wang, J.J. Chen, J.K. Marmon, M. Bhatt, S. Wozny, Y. Zhang, W. L. Zhou, Enhanced broad band photodetection through piezo-phototronic effect in CdSe/ZnTe core/shell nanowire array, Adv. Electron Mater. 1 (2015) 1400050.

[55] S.W. Xu, W.Q. Qian, D. Zhang, X. Zhao, X.M. Zhang, C.B. Li, C.R. Bowen, Y. Yang, A coupled photo-piezo-catalytic effect in a BST-PDMS porous foam for enhanced dye wastewater degradation, Nano Energy 77 (2020) 105305.